Original Research

Rapid Freehand MR-Guided Percutaneous Needle Interventions: An Image-Based Approach to Improve Workflow and Feasibility

Eva Rothgang, MS,[1,2*] Wesley D. Gilson, PhD,[2,3] Frank Wacker, MD,[3,4] Joachim Hornegger, PhD,[1] Christine H. Lorenz, PhD,[2,3] and Clifford R. Weiss, MD[3]

Purpose: To develop and evaluate software-based methods for improving the workflow of magnetic resonance (MR)-guided percutaneous interventions.

Materials and Methods: A set of methods was developed that allows the user to: 1) plan an entire procedure, 2) directly apply this plan to skin entry site localization without further imaging, and 3) place a needle under real-time MR guidance with automatic alignment of three orthogonal slices along a planned trajectory with preference to the principal patient axes. To validate targeting accuracy and time, phantom experiments (96 targets) and in vivo paraspinal and kidney needle punctures in two pigs (55 targets) were performed. The influence of trajectory obliquity, level of experience, and organ motion on targeting accuracy and time was analyzed.

Results: Mean targeting error was 1.8 ± 0.9 mm (in vitro) and 2.9 ± 1.0 mm (in vivo) in all directions. No statistically significant differences in targeting accuracy between single- and double-oblique trajectories, novice and expert users, or paraspinal and kidney punctures were observed. The average time (in vivo) from trajectory planning to verification of accurate needle placement was 6 minutes.

Conclusion: The developed methods allow for accurate needle placement along complex trajectories and are anticipated to reduce table time for MR-guided percutaneous needle interventions.

Key Words: interventional MRI; percutaneous interventions; MR-guided therapy; MR-guided interventions
J. Magn. Reson. Imaging 2013;37:1202–1212.

AN INCREASING NUMBER of percutaneous interventional procedures is being performed under magnetic resonance (MR) guidance (1) including aspiration (2–4), biopsy (3,5–16), sclerotherapy (17), targeted drug delivery (18–21), and thermal ablation (22–25). Its excellent soft-tissue contrast and multiplanar imaging capabilities make it an attractive alternative to computed tomography (CT) or ultrasound (US), in particular for targets in locations requiring a highly angulated approach and non-axial scan planes, such as hepatic dome or adrenal lesions, or lesions only visible with MR. However, over 20 years after the introduction of interventional MRI (iMRI) (2), these procedures are still performed primarily at academic hospitals. One of the barriers to more widespread adoption is the lack of a streamlined workflow and the complexity with respect to oblique and orthogonal slice prescriptions.

Although stereotactic methods exist (6,9,18,26–29), the freehand technique is the simplest and most common approach (4,8–14,19–21,24–25,30). It most closely approximates the typical workflow for CT or US-guided needle placements and requires no special equipment beyond an MR-compatible needle. The freehand technique is comprised of three basic steps: trajectory planning, skin entry point localization, and slice alignment for continuous needle visualization during placement.

Trajectory planning typically is performed by prescribing a single oblique trajectory using 2D images. However, not all lesions can be accessed with the entry point being in the same slice as the target point. Methods are therefore needed to improve double-oblique trajectory planning and review capabilities. Skin entry point localization in wide-bore MR scanners is usually performed by skin fiducials, eg, using an MR visible grid or capsule, or by creating an

[1]Friedrich Alexander University, Pattern Recognition Lab, Department of Computer Science, Erlangen, Germany.
[2]Siemens Corporate Research, Center for Applied Medical Imaging, Baltimore, Maryland, USA.
[3]Johns Hopkins University, Russell H. Morgan Department of Radiology and Radiological Science, Baltimore, Maryland, USA.
[4]Hannover Medical School, Department of Radiology, Germany.
Additional Supporting Information may be found in the online version of this article.
*Address reprint requests to: E.R., Friedrich-Alexander University Erlangen-Nuremberg, Pattern Recognition Lab (Informatik 5), Martensstr. 3, 91058 Erlangen, Germany.
E-mail: eva.rothgang@informatik.uni-erlangen.de
Received February 13, 2012; Accepted September 17, 2012.
DOI 10.1002/jmri.23894
View this article online at wileyonlinelibrary.com.

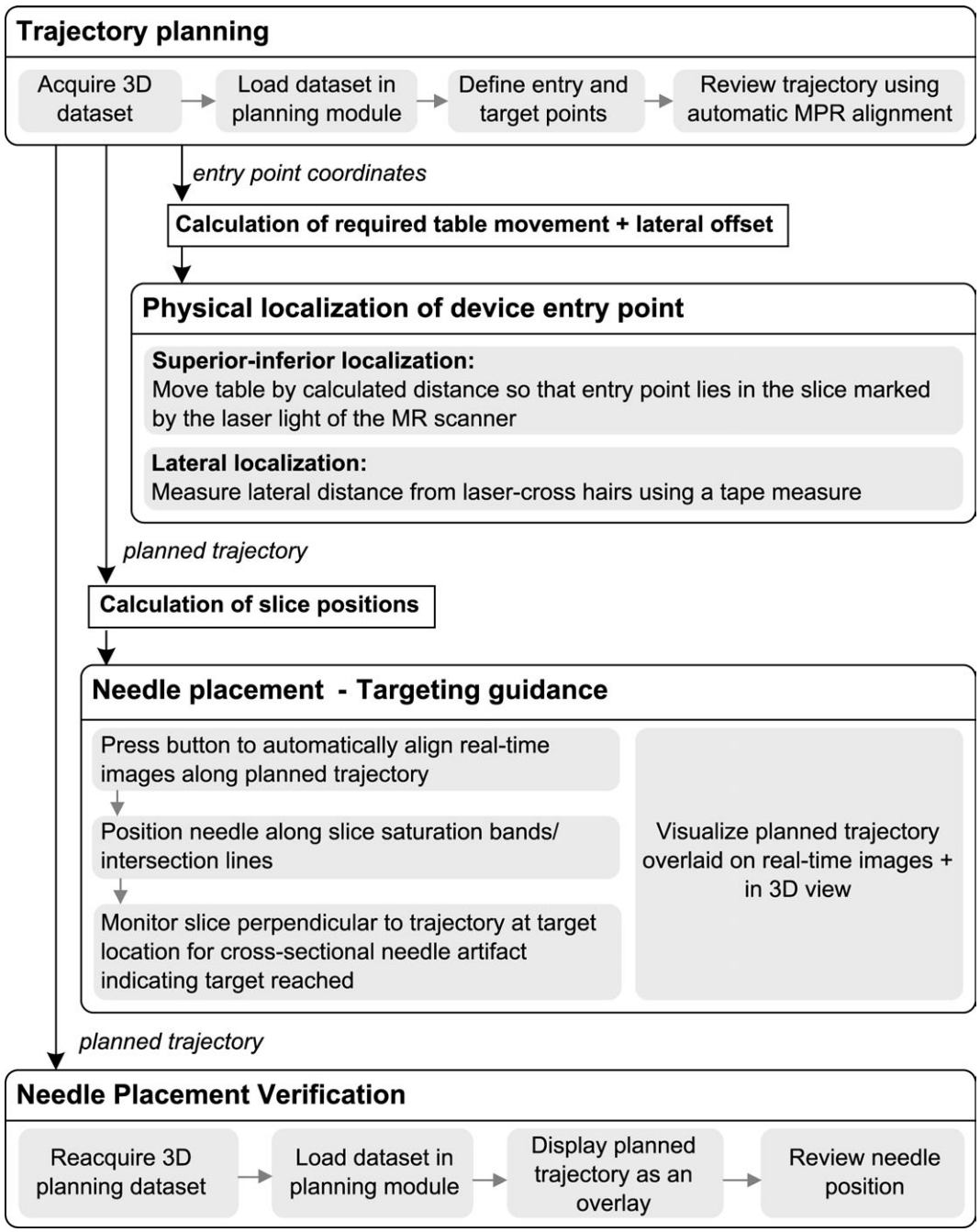

Figure 1. Proposed procedure workflow for rapid freehand MR-guided percutaneous needle placement. In a procedure where no precise measurement of targeting accuracy is necessary, the verification step could also be replaced by acquisition of a few slices around the lesion without the need for breath-hold.

artifact on the skin using a fingertip or water-filled syringe (3,10,14,20,30). This sounds straightforward, but it can be time-consuming due to its iterative nature and the need for additional imaging. Finally, it is essential to align imaging slices in order to continuously visualize the entire needle, the target lesion, and the surrounding anatomy during needle placement. However, manual slice alignment can be confusing and time-consuming for both the interventionalist and the MR technologist, in particular when complicated oblique or orthogonal image planes need to be prescribed (31,32).

These three essential steps often comprise the bulk of procedure time. Therefore, we hypothesized that procedure time, in particular for complex trajectories, can be reduced through rapid pre- and intraprocedure trajectory planning for multiple needle placements, combined with rapid identification of the skin entry site, and rapid slice plane alignment. Thus, our goal was to develop and validate methods to improve and streamline the workflow of MR-guided percutaneous procedures with a focus on target locations that cannot be easily reached using CT or US guidance.

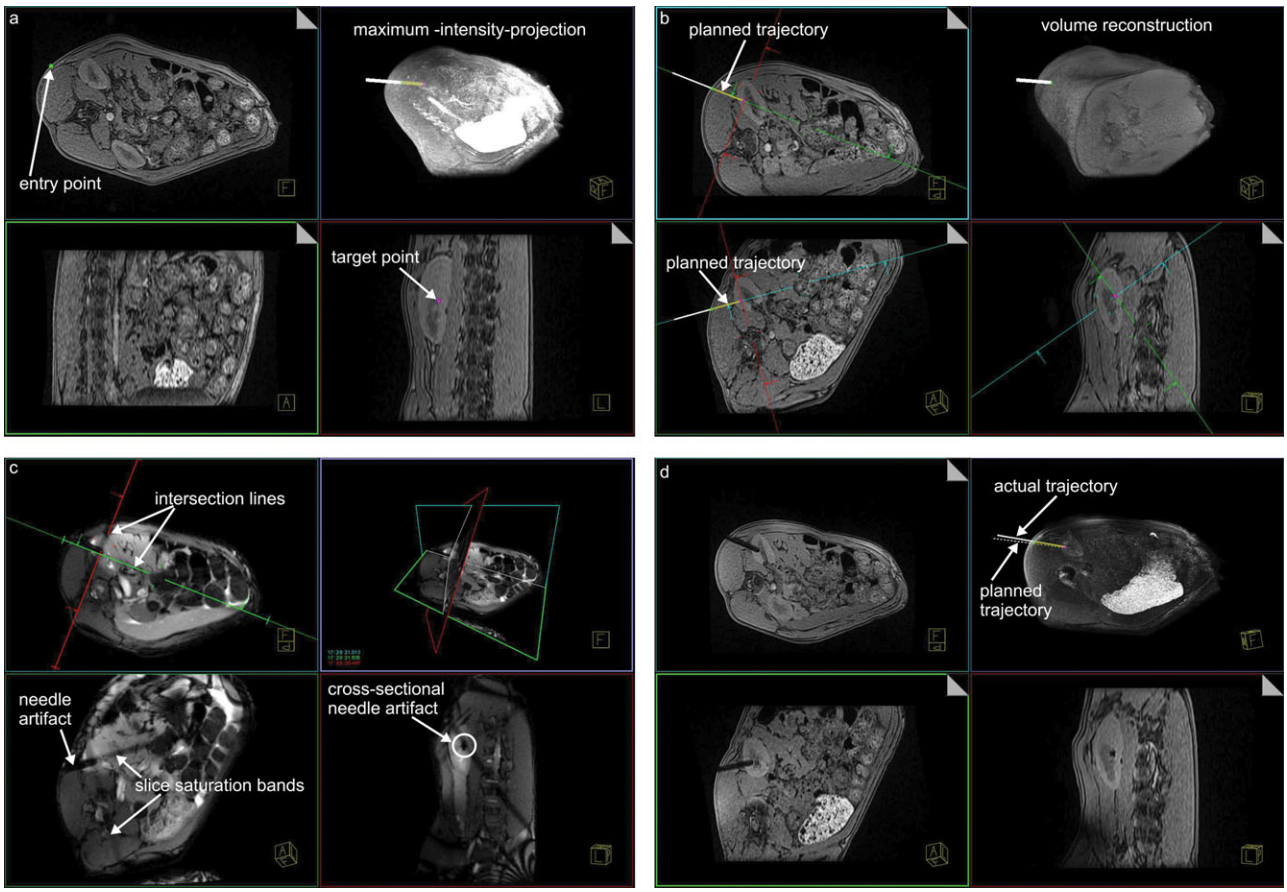

Figure 2. Placement of a needle along a double-oblique path into the kidney of a swine. **a:** Planning: Definition of trajectory by placing the entry and target point in two planes of different orientations. **b:** Trajectory review: Automatic alignment of MPR planes along planned trajectory for straightforward review of needle path. Magenta dot indicates planned target. **c:** Targeting: Needle placement under real-time MR imaging guided by the slice saturation bands and the intersection lines. The imaging planes are automatically aligned. The cross-sectional needle artifact in the plane perpendicular to the planned path at the target location indicates successful needle placement. **d:** Verification of needle position in comparison to the planned path.

MATERIALS AND METHODS

Procedure Workflow

Methods for each step of the workflow are shown in Fig. 1 and described below.

Trajectory Planning

A high-spatial resolution MR dataset is acquired (details in MRI Protocol section) and loaded into the planning application where the data can be displayed using multiplanar reformatting (MPR), maximum intensity projection (MIP), and volume rendering. The entry and target points are set using two mouse clicks, and the MPR planes are automatically aligned to the planned trajectory with two MPR planes along the needle and the third MPR plane orthogonal to the trajectory at the planned target location (see Auto Slice Alignment Algorithm section). This step supports reviewing the planned path to ensure avoidance of sensitive structures. This slice configuration is also useful for real-time MR-guided needle placement. (See also Fig. 2a, b and Supporting Movie 1.)

Entry Point Localization

The entry point on the subject's skin is physically identified in two steps (Figs. 1, 3). First, superior–inferior localization is performed by translating the MR scanner table such that the landmark laser delineates the z-coordinate of the prescribed entry point. Second, lateral localization is determined by measuring the L-R offset of the planned entry point (as determined by the planning software) from the laser crosshairs using an MR-compatible measuring tape.

For calculation of the required table movement, t_{move}, two cases need to be distinguished, as the coordinate system changes depending on the patient registration:

$$t_{move} = d_{iso,laser} + t_{curr\ pos} + \begin{cases} e_z \\ -e_z \end{cases} \quad patient\ registered \quad \begin{cases} head \\ feet \end{cases} \quad first \qquad [1]$$

$d_{isolaser}$ is the distance from the isocenter of the magnet to the laser light of the MR scanner, $t_{curr\ pos}$ is the current table position, and e_z is the z-coordinate of the planned entry point. The lateral offset $d_{lateral}$

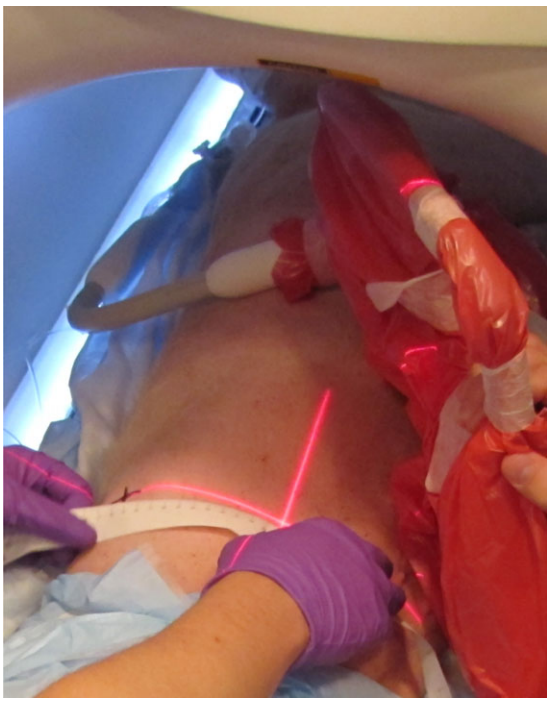

Figure 3. Physical entry point localization by moving the table by the determined distance and measuring the L-R offset of the planned entry point from the laser crosshairs using an MR-compatible measuring tape.

from the laser cross-hairs is given by the x-coordinate e_x of the planned entry point:

1. $d_{lateral} = |e_x|$ to the left if $e_x < 0$ and patient is registered head first or $e_x > 0$ and patient is registered feet first.
2. $d_{lateral} = |e_x|$ to the right if $e_x > 0$ and patient is registered head first or $e_x < 0$ and patient is registered feet first.

Needle Placement

For supporting identification of correct needle angulation, the planned trajectory is overlaid on the 3D view, which can be freely rotated to create a picture in mind of the spatial needle orientation. Prior to returning the patient table to the isocenter of the magnet, the skin entry point is prepared and the needle is partially inserted. Continuous real-time interactive imaging (2–5 fps) is used during needle advancement (details of acquisition in MRI Protocol section). Once triggered by the user, three MR-slices are automatically aligned to the planned path: two along and one orthogonal at the target. As a general guideline, these slices are oriented with preference to the standard axial, coronal, and sagittal planes (see Auto Slice Alignment Algorithm section). As a result of the intersecting acquisition slice planes, the resulting saturation bands correspond to the planned path and define the target location at the intersection of these bands. Moreover, successful placement of the needle is indicated as a cross-sectional needle artifact (33) appears in the orthogonal target slice. (See also Fig. 2c and Supporting Movie 2.)

If desired, it is further possible to adjust the planned needle path and realign the imaging planes during real-time imaging.

Needle Placement Verification

For validation of targeting accuracy, the actual needle position is compared to the planned trajectory by reacquiring the high-spatial-resolution MR dataset with the needle in position, loading it into the planning application, and overlaying the planned path. (See Fig. 2d and Supporting Movie 3.)

Auto Slice Alignment Algorithm

Auto slice alignment is used for both MPR alignment for trajectory review during planning and real-time scan plane alignment during targeting. The configuration for auto slice alignment is as follows: two slices along the planned path d_p orthogonal to each other and the third slice orthogonal to the trajectory at the planned target location. The slices are oriented so that they are most closely aligned to the standard axial, coronal, and sagittal planes which span the patient coordinate system. The standard axial plane is defined by the row vector $r_1 = (1,0,0)^T$, the column vector $c_1 = (0,1,0)^T$, and the normal $n_1 = (0,0,1)^T$; the standard coronal plane by $r_2 = (1,0,0)^T$, $c_2 = (0,0,-1)^T$, and $n_2 = (0,1,0)^T$; and the standard sagittal plane by $r_3 = (0,1,0)^T$, $c_3 = (0,0,-1)^T$, and $n_3 = (-1,0,0)^T$. The planned path d_p is defined by $d_p = t_p - e_p$, where $e_p \in \mathrm{R}^3$ is the entry point and $t_p \in \mathrm{R}^3$ the target point. The automatic slice alignment algorithm with preference to the standard axial, coronal, and sagittal planes works as follows:

1. Determine how close each standard plane is to the planned path d_p. The two closest ones are used for the two slices along the planned path, the third one is used as the orthogonal one.
2. Span the first slice along the planned path by the vectors $v_{1,1} = d_p$ and $n_i \times d_p$, where n_i is the normal of the closest standard plane.
3. Ensure default slice orientation so that its r, c, and n vectors point in the same direction as the r, c, and n vectors of the corresponding standard axial, coronal, or sagittal plane.
4. In order to minimize wrap artifacts for a given field of view, the center g of the slice is translated so that the normal through its center coincides with the center g_0 of the volume dataset. The new center g_{new} of the slice can be calculated by $g_{new} = g + \mu r + \xi c$, where $\mu = (g_0 - g)^T \cdot r$ and $\xi = (g_0 - g)^T \cdot c$.
5. Span the second slice along the planned path orthogonal to the first one by the vectors $v_{2,1} = d_p$ and $v_{2,2} = v_{1,2} \times d_p$. Apply steps 3 and 4 accordingly.
6. Align the third slice orthogonal to the first two ones intersecting at the target point by setting $v_{3,1} = v_{1,1} \times v_{1,2}$ and $v_{3,2} = v_{1,2} \times v_{2,2}$. Set the center of the slice to the target point and apply step 3 accordingly.

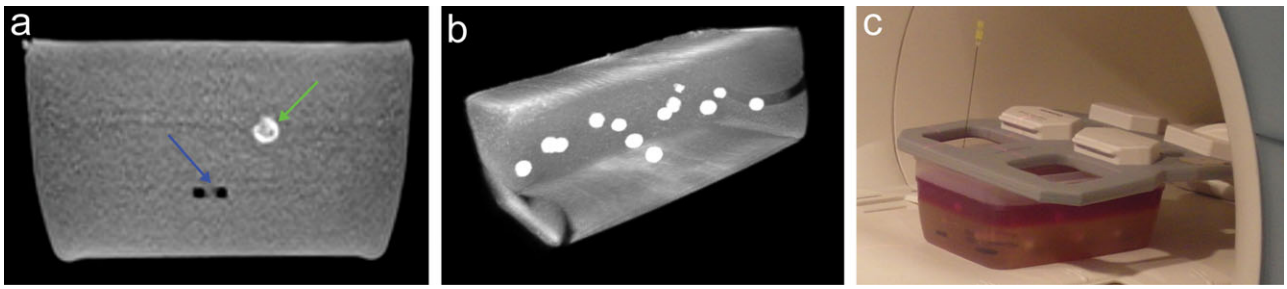

Figure 4. Axial MR image **(a)**, maximum intensity projection **(b)**, and photograph **(c)** of gelatin phantom with embedded O-rings (blue arrow) as targets and wooden beads (green arrow) to mimic vital structures.

Implementation

For validation, the described methods were implemented as planning and guidance modules within the Interactive Front End (IFE), a real-time MR-scanner control system interface (34). Further examples for such interfaces can be found elsewhere (35).

MRI Protocol

MRI was performed on a wide-bore 1.5T MR-scanner (Magnetom Espree, Siemens Healthcare, Erlangen, Germany) using the 6-element body matrix coil combined with six elements of the spine matrix coil. The real-time navigation user interface was projected onto a screen in the scanner room (Fig. 6) to provide live feedback about the current needle position to the user.

The imaging protocol consisted of 1) acquisition of a 3D planning dataset by using a 3D T1-weighted gradient echo sequence (VIBE, volumetric interpolated breath-hold examination); 2) real-time imaging during the procedure using a real-time, interactive, multislice balanced SSFP sequence (36); 3) reacquisition of 1) with the needle in place for validation of needle position with respect to the planned path.

For the phantom experiments, VIBE images were acquired in 41 seconds covering 144 slices (4.88 msec repetition time [TR], 2.38 msec echo time [TE], 10° flip-angle, 2 mm slice thickness, 140 × 200 mm field of view [FOV], 112 × 160 matrix). For the animal experiments, 104–128 slices were acquired under breath-hold conditions in 35–38 seconds (5 msec TR, 2 msec TE, 9° flip-angle, 2 mm slice thickness, [233-250] × [320–340] mm FOV, [352–400] × 512 matrix).

The needles were placed during free-breathing using real-time, multislice interactive imaging (4.6 msec TR, 2.3 msec TE, 60° flip angle, 5–10 mm slice thickness, 300 × 300 mm FOV, 192 × 192 matrix, imaging time of 0.5 seconds per plane). All real-time and VIBE imaging was performed with GRAPPA (37) acceleration factor 2 and reference lines 24.

Phantom Experiments

Ninety-six needle (20G, 20 cm Chiba MReye biopsy needle; Cook, Bloomington, IN) punctures were performed in a custom-designed stiff gelatin phantom (36 g per 500 ml pure water) with 12 embedded rubber O-rings (8 mm inner diameter). Twelve wooden beads (12 mm diameter) were also embedded to mimic vital structures to be avoided during the insertions. A layer of red gelatin was pored on top to obstruct visibility of targets by the user from above. See Fig. 4 for details of the phantom.

Following the proposed procedure workflow, two expert interventionalists (5 and 15 years of experience) and two nonexpert users (no interventional experience) selected and planned a single-oblique and a double-oblique trajectory for each target (24 needle insertions per user), reviewed the planned path to avoid the beads, localized the entry point on the phantom, and inserted the needle along the planned path into the defined target point. A 3D validation dataset was acquired after each insertion with the needle still in place to verify the needle position with respect to the planned path and target point. Trajectory lengths ranged between 64 and 116 mm.

Animal Experiments

The protocol for animal experiments was approved by the local Institutional Animal Care and Use Committee. Fifty-five needle (20G, 20 cm Chiba MReye) insertions were performed by an expert interventionalist in two living pigs (45–50 kg). The animals were initially sedated with an intramuscular injection of dexmedetomidine 0.8–1 mL and ketamine, 10 mg/kg, then intubated and maintained on a mechanical ventilator with inhaled 1%–1.5% isoflurane. The animals were positioned on the MR-scanner table prone or decubitus.

Twenty points in the paraspinal muscles of the two pigs were selected as targets. To validate our methods in a moving organ, 35 target points were further selected in all segments of the kidney. The task was to insert the needle into the target point following the planned trajectory. The planned path, entry, and target points could be displayed as overlays on the real-time images.

Following the proposed procedure workflow, the interventionalist first planned and reviewed the trajectory to the defined target point. Depending on the target location, the trajectory was planned within a single slice plane (single-oblique) or using two planes (double-oblique). Trajectory lengths ranged between 30 and 88 mm. The needle insertions were planned in groups of five to mimic a complicated procedure and

Table 1
Targeting Accuracy and Time

		Mean targeting error (mm)			
		In-plane			
		X	y	Out-of-plane	Mean targeting time (min:sec)
Phantom – Single oblique paths					
Novice users	$n = 24$	1.3 (± 1.0)	1.7 (± 1.5)	1.9 (±1.5)	1:46 (±0:36)
Expert users	$n = 24$	2.1 (±1.6)	1.8 (±1.3)	1.2 (±1.0)	1:08 (±0:35)
Phantom – Double oblique paths					
Novice users	$n = 24$	1.6 (±1.3)	2.2 (±1.9)	1.9 (±1.3)	2:04 (±0:47)
Expert users	$n = 24$	1.8 (±1.4)	1.7 (±1.0)	2.7 (±2.0)	1:42 (±1:02)
Phantom – All					
All paths	$n = 96$	1.7 (±1.4)	1.9 (±1.4)	1.9 (±1.6)	1:40 (±0:50)
In vivo – Single oblique paths					
Paraspinal	$n = 10$	2.7 (±0.6)	2.4 (±1.7)	3.0 (±2.1)	1:23 (±0:30)
Kidney	$n = 13$	3.7 (±1.6)	4.2 (±1.9)	2.1 (±1.8)	1:31 (±0:43)
In vivo – Double oblique paths					
Paraspinal	$n = 10$	2.5 (±2.3)	4.1 (±2.0)	2.1 (±1.3)	2:09 (±0:56)
Kidney	$n = 22$	3.4 (±1.7)	2.5 (±1.8)	2.2 (±2.0)	2:19 (±1:18)
In vivo –All					
All paths	$n = 55$	3.2 (±1.7)	3.2 (±2.0)	2.3 (±1.9)	1:53 (±0:57)

Numbers in parentheses are standard deviations.

to allow for assessment of procedure time for multiple needle placements in a single patient. During free breathing, the needles were inserted in a single advancement into the target point, 10 along single-oblique and 10 along double-oblique trajectories for the paraspinal targets, and 13 along single-oblique and 22 along double-oblique trajectories for the targets in the kidney. A 3D validation dataset was acquired after each insertion with the needle still in place to verify the needle position with respect to the planned path and target point.

Data Analysis

For evaluation of targeting accuracy in phantom and animal experiments, the needle centerline was manually segmented in each 3D verification dataset by selecting the entry and target point (consensus by three observers). In-plane and out-of-plane errors were calculated by comparing the 3D coordinates of the segmented needle centerlines and the 3D coordinates of the corresponding planned trajectories. Two-way analysis of variance (ANOVA) on targeting accuracy in the phantom and in vivo organs (paraspinal muscle, kidney) was performed with one factor being trajectory obliquity (single-, double-oblique) and the other factor being the level of expertise (nonexpert, expert).

Time needed for preprocedure imaging, planning, entry point localization, targeting, and verification imaging was recorded. As the assumption of normality was not met for targeting time, the nonparametric Kruskal–Wallis test was used to analyze differences in targeting time for single- versus double-oblique trajectories, nonexpert versus expert users for the phantom experiments, and paraspinal versus kidney for the animal experiments. Linear regression was performed to analyze trajectory length versus targeting error. All evaluations were performed with MatLab (MathWorks, Natick, MA). A significance level of $P < 0.05$ was used.

Clinical Feasibility

Approved by the local Institutional Review Board and with written consent from the patient, the system was used to guide needle placement for percutaneous sclerotherapy of a complex intraperitoneal venous malformation involving the mesentery of a 40-year-old woman. The patient had already undergone one successful sclerotherapy of some superficial portions of this lesion using standard ultrasound and x-ray fluoroscopic guidance, but subsequent attempts to treat the deeper lesions using these modalities had failed. Four needles were placed following the proposed procedure workflow and relevant procedure times were recorded.

RESULTS

Phantom Experiments

All 96 targets were successfully punctured with a mean targeting error of 1.8 ± 1.5 mm (standard deviation) in all directions. Detailed results are given in Table 1. Two-way ANOVA showed no significant difference in targeting accuracy between nonexpert and expert users ($P = 0.36$) or between single- and double-oblique paths ($P = 0.19$). No interaction effect between level of expertise and trajectory obliquity on targeting accuracy was found ($P = 0.85$). The mean 3D distance between the actual entry point and the planned trajectory was 3.9 ± 2.3 mm.

The mean skin to target time was 100 ± 50 seconds. The Kruskal–Wallis test revealed a significant difference in targeting time between single- and double-oblique paths ($P = 0.03$). Expert users were significantly faster than nonexpert users for single-oblique paths ($P = 0.03$) but not for double-oblique paths ($P = 0.18$). The median path length for single-oblique paths was 71 mm (range, 64–94 mm) and 79 mm (range,

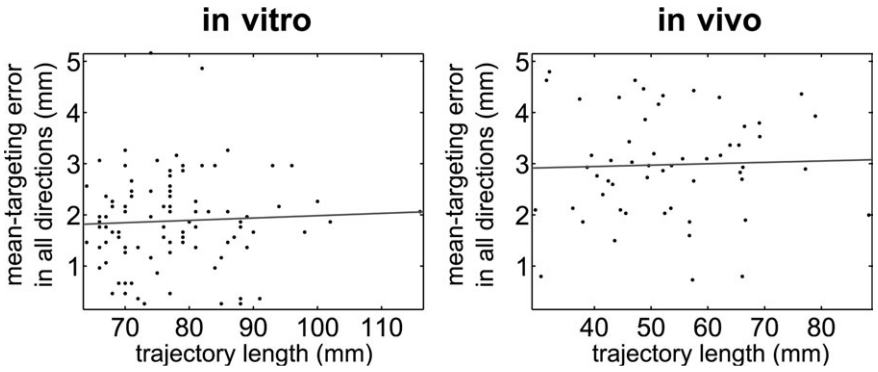

Figure 5. Targeting error is independent of trajectory length for both in vitro (left) and in vivo (right). The solid lines represent the linear regression fits.

66–116 mm) for double-oblique paths. As illustrated in Fig. 5, no relation could be found between path length and targeting error.

Animal Experiments

All 55 needles were successfully placed into the selected target points with a mean error of 2.9 ± 1.9 mm in all directions. Detailed results are given in Table 1. Two-way ANOVA showed no significant difference in targeting accuracy between paraspinal and kidney insertions ($P = 0.26$) or between single- and double-oblique trajectories ($P = 0.90$). There was no significant interaction effect between targeted organ and trajectory obliquity on targeting accuracy ($P = 0.14$). The mean 3D distance between the actual entry point (ie, skin nick) and the entry point of the planned trajectory was 5.1 ± 2.6 mm.

The mean intervention time from acquisition of planning images to verification of correct needle placement was 6 minutes. The mean skin-to-target time was 113 ± 57 seconds, with further details on the components of the procedure times given in Table 2. The Kruskal–Wallis test showed no significant difference in targeting time between paraspinal and kidney insertions ($P = 0.80$) but a significant difference between single- and double-oblique trajectories ($P = 0.003$). The median path length was 49 mm (range, 30–69 mm) for single-oblique paths and 55 mm (range, 31–88 mm) for double-oblique paths. As illustrated in Fig. 5, the targeting error was independent of the path length.

First Clinical Experience

All four needles were successfully placed into the venous malformation (Fig. 6), and the therapeutic agent (gadolinium DTPA-doped 3% sodium tetradecyl sulfate) was administered without extravasation or complication. Total time related to needle placement was 16 minutes (see Table 2). The mean skin to target time was 76 ± 30 seconds with a median path length of 103 mm (range, 84–122 mm).

Table 2
Procedure Time for In Vivo Studies

		Time	
Parameter		Animal	Patient
Preprocedure imaging time (scout images + planning dataset)		70 sec	172 sec
Mean planning time		6 min (±2) (5 needles)	4 min (4 needles)
Entry point localization time		< 60 sec	
Mean skin to target time per needle		113 sec (±57)	76 sec (±30)
Verification imaging time		41 sec	23 sec
		Total intervention time*	
Animal 1	Procedure 1 – Paraspinal	26 min	5 needles per procedure
	Procedure 2 – Paraspinal	26 min	
	Procedure 3 – Kidney	24 min	
	Procedure 4 – Kidney	23 min	
	Procedure 5 – Kidney	27 min	
Animal 2	Procedure 6 – Paraspinal	23 min	5 needles per procedure
	Procedure 7 – Paraspinal	18 min	
	Procedure 8 – Kidney	24 min	
	Procedure 9 – Kidney	22 min	
	Procedure 10 – Kidney	18 min	
	Procedure 11 – Kidney	21 min	
Patient	Abdominal	16 min	4 needles

*Includes planning, entry point localization, targeting, and verification.

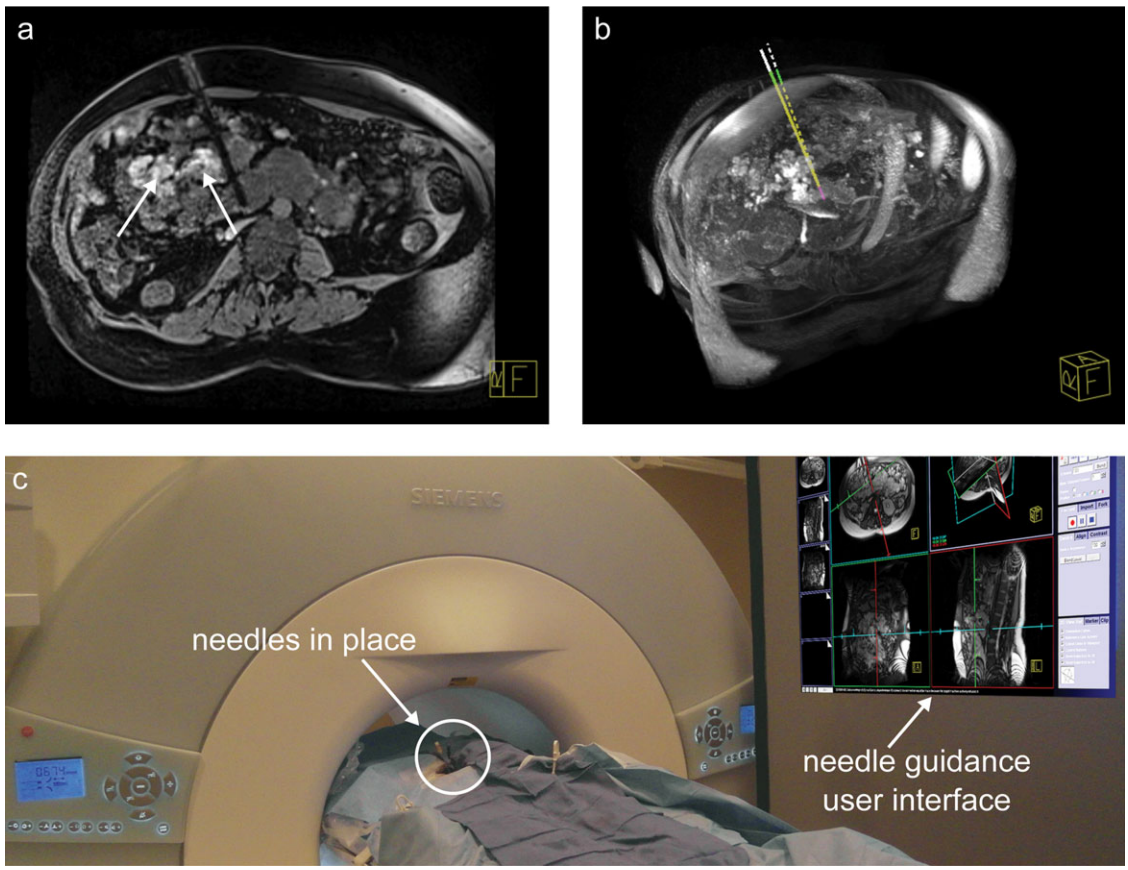

Figure 6. Successful needle placements (four needles) for sclerotherapy of a complex intraperitoneal venous malformation (VM) in a 40-year-old woman with Klippel–Trénaunay syndrome who had failed ultrasound and x-ray fluoroscopy-guided treatment. **a:** Verification dataset of needle placement into a VM adjacent to vena cava and other critical structures. Areas of the VM treated earlier in this procedure with gadolinium DTPA-doped 3% sodium tetradecyl sulfate still show enhancement in the image (arrows). **b:** Comparison between planned (dashed line) and actual needle trajectory. **c:** Patient in the scanner with needle guidance user interface displayed on a screen in the MR scanner room.

DISCUSSION

Software methods are presented that have the potential to simplify the key workflow steps of MR-guided needle interventions, in particular for complicated trajectories. This simplification of workflow overcomes many of the potential barriers to percutaneous needle interventions without extra hardware, such as tracking cameras (6,18,29), needle guides (26), or augmented reality overlay systems (9,27) that can disrupt and complicate the interventionalist's normal workflow and contribute to increased total intervention time (32). Using a purely software-based approach that does not require any setup time, less than 30 minutes (from planning to verification) was needed to place five needles in the kidney or spinal muscle of pigs (on average 6 minutes per needle) and approximately 16 minutes to place four needles in a patient abdomen. These are very reasonable times in comparison to what has been reported in the literature for manual MR-guided percutaneous interventions (Table 3).

For planning, the ability to prescribe multiple trajectories at one time allows the user to proceed from one needle placement to the next without the need to break scrub for planning or to identify the next skin entry site. This has been reported as a limitation of other systems (32). Multiplanar reformatting also allows for complex trajectory selection and when combined with automatic MPR plane alignment can enhance safety by providing advanced reviewing capabilities to ensure avoidance of critical structures. Furthermore, intraprocedure trajectory adjustments can be made without the need for needle repositioning.

Skin entry point localization is improved by automatically providing information regarding superior–inferior and lateral localization without the need to read out slice positions or measure distances in the images. Using only the MR system's laser and a tape measure, all skin entry sites can be accurately (within 5 mm) located before scrubbing the patient, and the interventionalist can move quickly from one site to the next without needing to reidentify entry sites and trajectories for each needle placement. The proposed real-time slice layout with two orthogonal slices along the planned trajectory further allows verifying correct needle angulation by using, eg, an MR visible tube over the needle, as the tube can only be seen in both longitudinal images when the needle is correctly oriented.

Table 3
In Vivo Studies on Manual MR-Guided Percutaneous Interventions in Abdominal Target Locations: Comparison of Reported Times

Author	Method	Organ	Time
High field			
Fischbach et al 2011 (14)	in-bore, freehand 1T Panorama, Philips	liver (50)	mean intervention time (planning to verification): 18 min (range, 15–35 min)
Hoffmann et al 2011 (16)	in-bore, freehand 1.5T MAGNETOM Espree, Siemens	liver (19), soft-tissue (19)	mean planning time: 64 min (liver); 43 min (soft-tissue) mean puncture time (needle insertion to retraction): 18 min (soft-tissue); 43 min (liver)
Busse et al 2010 (29)	out-of-bore, optical tracking 1.5T MAGNETOM Symphony, Siemens	scapula (1)	technical setup: 5 min patient positioning: 10 min planning (marker and roadmap images acquisition): 9 min
Das et al 2010 (12)	in-and-out, * freehand 1.5T MAGNETOM Avanto, Siemens	liver (4), pancreas (4), retroperi-toneum (2)	mean total procedure time: 59.7 min (range, 46–70 min); intervention time: 20–25 min
Kühn et al 2010 (13)	in-and-out, freehand 3T MAGNETOM Trio, Siemens	liver (47), spleen (1), kidney (2)	median intervention time (needle insertion to retraction): 9.3 min ± 8.1
Ricke et al 2010 (24)	in-bore, freehand 1T Panorama, Philips	liver (224)	mean intervention time (planning to dosimetry data acquisition): 64 min (range, 29–174 min)
Streitparth et al 2010 (21)	in-bore, freehand 1T Panorama, Philips	nerve root (107), facet (53), sacroiliac joint (23)	mean procedure time: 29 min (range, 19–67 min)
Fritz et al 2009 (20)	in-bore, freehand 1.5T MAGNETOM Espree, Siemens	nerve root (22), facet (18), epidural (9)	mean table time: 36 min (range, 23–75 min) mean real-time MRI: 38 sec (range, 12–185 sec)
Fritz et al 2008 (19)	in-bore, freehand 1.5T MAGNETOM Espree, Siemens	sacroiliac joint (60)	mean intervention time (entry point localization to needle retraction): 22.5 min (range, 5.0–67.5 min)
Stattaus et al 2008 (10)	in-bore, freehand 1.5T MAGNETOM Espree, Siemens	liver (20)	median puncture time (finger-pointing to needle placement): 19 min (range, 12–43 min)
Wacker et al 2006 (9)	out of bore, augmented reality 1.5T MAGNETOM Espree, Siemens	3 pigs	mean puncture time (planning to verification): 13 min
Low field			
Zangos et al 2006 (8)	in-bore, freehand 0.2T MAGNETOM Concerto, Siemens	paraaortic (20), kidney (2), adrenal gland (3), pancreas (5)	median intervention time (needle insertion to retraction): 12.3 min (range, 6.3–16.8 min)
Sakarya et al 2003 (4)	in-bore, freehand 0.3T Airis I, Hitachi	lung (14)	mean biopsy duration (planning to needle placement): 19 min (range, 15–28 min)
Genant et al 2002 (30)	in-bore, freehand 0.5T Signa SP, GE	spine + paraspinal (14), pelvic (17), upper extremities (13), foot and ankle (7), knee and leg (6), miscellaneous (6)	mean needle time (needle insertion to retraction): 26.2 min ± 19.7.
Ojala et al 2002 (6)	in-bore, optical tracking 0.23T Panorama, Philips	bone (5)	procedure time (needle insertion to retraction): < 40 min
Sequeiros et al 2002 (18)	in-bore, optical tracking 0.23T Panorama, Philips	nerve root (61)	mean puncture time (needle insertion to retraction): 12 min (range, 2–60 min)

*The patient is moved out from the bore to reposition the needle between scans.

Automatic slice alignment overcomes one of the challenges in a freehand MR-guided needle intervention (10). Because it is essential to continuously visualize the entire needle, the target, and the surrounding structures, slice alignment typically requires significant intraprocedure communication (14). This can be confusing and time-consuming for both the interventionalist and MR technologist, and is particularly challenging for complex trajectories (31,32). Unlike other studies which use only one (5,10,19,20)

Table 4
In Vitro Studies on Manual MR-Guided Percutaneous Interventions: Comparison of Reported Targeting Accuracies

Author	Method	Accuracy
Busse et al 2010 (29)	optical tracking	mean in-plane error: 3.1 mm (range, 1.0–5.8 mm) mean out-of-plane error: 4.5 mm (range, 2.0–7.0 mm)
Fischer et al 2007 (27)	freehand	mean in-plane error: 5.2 mm ± 5.56 mean orientation error: 4.07° ± 4.11
	protractor	mean in-plane error: 5.37 mm ± 7.36 mean orientation error: 3.35° ± 3.34
	laser	mean in-plane error: 2.90 mm ± 2.62 mean orientation error: 2.02° ± 2.22
	overlay	mean in-plane error: 2.00 mm ± 1.70 mean orientation error: 2.41° ± 2.27
Christoforou et al 2007 (26)	manipulator-driven	mean 3D error: 3.2 mm mean orientation error: 2.5°
Wacker et al 2006 (9)	augmented reality	mean minimum in-plane distance: 1.44 mm mean out-of-plane error: 2.55 mm

or two alternating imaging planes (14,21,24) during guidance, our strategy automatically prescribes three real-time imaging planes: two perpendicular planes along the needle path and a third orthogonal to them at the target location. Intuitive slice orientation is further improved by automatically aligning the slices as closely as possible to the principal patient axes. This orientation strategy gives the interventionalist the ability to quickly determine and correct deviations. Furthermore, intraprocedural adjustments of real-time imaging planes can be made by either adjusting the planned trajectory or slice planes without the need to stop scanning.

Targeting accuracy is essential for successful image-guided therapy, and an in-plane error of 5 mm is clinically acceptable in most situations. This study evaluated not only the in-plane error but also the out-of-plane error for both phantom and in vivo studies, and showed that nonexpert users were able to perform needle insertions within this accuracy limit even for double-oblique trajectories (Table 1). Only two of the in vivo studies on manual MR-guided percutaneous interventions listed in Table 3 report targeting accuracy. Our results are equivalent to the median lateral deviation of 3.4 mm found by Stattaus et al (10) and significantly better than the 3D targeting error of 9.6 mm reported using augmented reality guidance (9). Moreover, our needle placement accuracy in phantoms is in the same range as reported by others for stereotactic methods and significantly better than for the freehand approach (Table 4).

A limitation of the study relates to the validation of the targeting accuracy based on the manual segmentation of the needle artifact, which can vary depending on the needle composition, needle orientation to B0 and on several scan-related parameters (33). However, this potential source of error was mitigated by using a highly resolved 3D validation dataset, which should be more accurate than 2D measurements in one plane (10,15) and by consensus approval of all segmentations by three users blinded to the initial planned trajectory. Another limitation of the study is that a control arm without the use of the proposed methods was not performed. It should also be noted that freehand MR-guided interventions such as the one presented in this study benefit greatly from open or wide-bore (70 cm) MR scanners, as patient access in the magnet is challenging and needle advancement in a 60-cm bore is difficult.

In conclusion, the presented methods allow for a streamlined workflow that approximates a "typical" (non-MR) image-guided percutaneous interventional procedure without introducing additional navigation hardware, and allows users to rapidly and accurately perform these interventions radiation-free using only real-time MR guidance. These methods hold promise for facilitating the adoption of MR-guidance of percutaneous needle interventions beyond academic centers and are in particular attractive for complicated trajectories that are not easily achieved using CT or US guidance.

ACKNOWLEDGMENTS

We thank the team of the Center for Applied Medical Imaging, Siemens Corporate Research, for support and Steffi Valdeig for support with the animal experiments.

REFERENCES

1. Tatli S, Morrison PR, Tuncali K, Silverman SG. Interventional MRI for oncologic applications. Tech Vasc Interv Radiol 2007;10:159–170.
2. Mueller P, Stark D, Simeone J, et al. MR-guided aspiration biopsy: needle design and clinical trials. Radiology 1986;161:605–609.
3. Lewin JS, Nour SG, Duerk JL. Magnetic resonance image-guided biopsy and aspiration. Top Magn Reson Imaging 2000;11:173–183.
4. Sakarya ME, Unal O, Ozbay B, et al. MR fluoroscopy-guided transthoracic fine-needle aspiration biopsy: feasibility. Radiology 2003;228:589–592.
5. Silverman SG, Collick BD, Figueira MR, et al. Interactive MR-guided biopsy in an open-configuration MR imaging system. Radiology 1995;197:175–181.
6. Ojala R, Sequeiros RB, Klemola R, Vahala E, Jyrkinen L, Tervonen O. MR-guided bone biopsy: preliminary report of a new guiding method. J Magn Reson Imaging 2002;15:82–86.
7. Beyersdorff D, Winkel A, Hamm B, Lenk S, Loening SA, Taupitz M. MR Imaging-guided prostate biopsy with a closed MR unit at 1.5 T: initial results. Radiology 2005;234:576–581.

8. Zangos S, Eichler K, Wetter A, et al. MR-guided biopsies of lesions in the retroperitoneal space: technique and results. Eur Radiol 2006;16:307–312.
9. Wacker FK, Vogt S, Khamene A, et al. An augmented reality system for MR image-guided needle biopsy: initial results in a swine model. Radiology 2006;238:497–504.
10. Stattaus J, Maderwald S, Forsting M, Barkhausen J, Ladd ME. MR-guided core biopsy with MR fluoroscopy using a short, wide-bore 1.5-Tesla scanner: feasibility and initial results. J Magn Reson Imaging 2008;27:1181–1187.
11. Weiss CR, Nour SG, Lewin JS. MR-guided biopsy: a review of current techniques and applications. J Magn Reson Imaging 2008; 27:311–325.
12. Das CJ, Goenka AH, Srivastava DN. MR-guided abdominal biopsy using a 1.5-Tesla closed system: a feasibility study. Abdom Imaging 2010;35:218–223.
13. Kühn JP, Langner S, Hegenscheid K, et al. Magnetic resonance-guided upper abdominal biopsies in a high-field wide-bore 3-T MRI system: feasibility, handling, and needle artefacts. Eur Radiol 2010;20:2414–2421.
14. Fischbach F, Bunke J, Thormann M, et al. MR-guided freehand biopsy of liver lesions with fast continuous imaging using a 1.0-T open MRI scanner: experience in 50 patients. Cardiovasc Intervent Radiol 2011;34:188–192.
15. Zangos S, Melzer A, Eichler K, et al. MR-compatible assistance system for biopsy in a high-field-strength system: initial results in patients with suspicious prostate lesions. Radiology 2011;259: 903–910.
16. Hoffmann R, Thomas C, Rempp H, et al. Performing MR-guided biopsies in clinical routine: factors that influence accuracy and procedure time. Eur Radiol 2012;22:663–671.
17. Boll DT, Merkle EM, Lewin JS. Low-flow vascular malformations: MR-guided percutaneous sclerotherapy in qualitative and quantitative assessment of therapy and outcome. Radiology 2004;233: 376–384.
18. Sequeiros RB, Ojala RO, Klemola R, Vaara TJ, Jyrkinen L, Tervonen OA. MRI-guided periradicular nerve root infiltration therapy in low-field (0.23-T) MRI system using optical instrument tracking. Eur Radiol 2002;12:1331–1337.
19. Fritz J, Henes JC, Thomas C, et al. Diagnostic and interventional MRI of the sacroiliac joints using a 1.5-T open-bore magnet: a one-stop-shopping approach. Am J Roentgenol 2008;191: 1717–1724.
20. Fritz J, Thomas C, Clasen S, Claussen CD, Lewin JS, Pereira PL. Freehand real-time MRI guided lumbar spinal injection procedures at 1.5 T: feasibility, accuracy, and safety. Am J Roentgenol 2009;193:W161–W167.
21. Streitparth F, Walter T, Wonneberger U, et al. Image-guided spinal injection procedures in open high-field MRI with vertical field orientation: feasibility and technical features. Eur Radiol 2010; 20:395–403.
22. Nour SG, Goldberg SN, Wacker FK, et al. MR monitoring of NaCl-enhanced radiofrequency ablations: observations on low-and high-field-strength MR images with pathologic correlation. Radiology 2010;254:449–459.
23. Morrison PR, Silverman SG, Tuncali K, Tatli S. MRI-guided cryotherapy. J Magn Reson Imaging 2008;27:410–420.
24. Ricke J, Thormann M, Ludewig M, et al. MR-guided liver tumor ablation employing open high-field 1.0 T MRI for image-guided brachytherapy. Eur Radiol 2010;20:1985–1993.
25. Wacker FK, Cholewa D, Roggan A, Schilling A, Waldschmidt J, Wolf KJ. Vascular lesions in children: percutaneous MR imaging-guided interstitial Nd: YAG laser therapy — preliminary experience. Radiology 1998;208:789–794.
26. Christoforou E, Akbudak E, Ozcan A, Karanikolas M, Tsekos NV. Performance of interventions with manipulator-driven real-time MR guidance: implementation and initial in vitro tests. Magn Reson Imaging 2007;25:69–77.
27. Fischer GS, Deguet A, Csoma C, et al. MRI image overlay: application to arthrography needle insertion. Comput Aided Surg 2007;12:2–14.
28. Moche M, Trampel R, Kahn T, Busse H. Navigation concepts for MR image-guided interventions. J Magn Reson Imaging 2008;27: 276–291.
29. Busse H, Garnov N, Thörmer G, et al. Flexible add-on solution for MR image-guided interventions in a closed-bore scanner environment. Magn Reson Med 2010;64:922–928.
30. Genant JW, Vandevenne JE, Bergman AG, et al. Interventional musculoskeletal procedures performed by using MR imaging guidance with a vertically open MR unit: assessment of techniques and applicability. Radiology 2002;223:127–136.
31. Stattaus J, Maderwald S, Baba HA, et al. MR-guided liver biopsy within a short, wide-bore 1.5 Tesla MR system. Eur Radiol 2008; 18:2865–2873.
32. Moche M, Zajonz D, Kahn T, Busse H. MRI-guided procedures in various regions of the body using a robotic assistance system in a closed-bore scanner: preliminary clinical experience and limitations. J Magn Reson Imaging 2010;31:964–974.
33. Lewin JS, Duerk JL, Jain VR, Petersilge CA, Chao CP, Haaga JR. Needle localization in MR-guided biopsy and aspiration: effects of field strength, sequence design, and magnetic field orientation. Am J Roentgenol 1996;166:1337–1345.
34. Lorenz CH, Kirchberg KJ, Zuehlsdorff S, et al. Interactive FrontEnd (IFE): A platform for graphical MR scanner control and scan automation. In: Proc 13th Annual Meeting ISMRM, Miami; 2005 (abstract 2170).
35. Yutzy, S, Duerk, J. Pulse sequences and system interfaces for interventional and real-time MRI. J Magn Reson Imaging 2008; 27:267–275.
36. Pan L, Barbot J, Shea S, et al. An integrated system for catheter tracking and visualization in MR-guided cardiovascular interventions. In: Proc 19th Annual Meeting ISMRM, Montréal; 2011 (abstract 195).
37. Griswold, M, Jakob, P, Heidemann, R, et al. Generalized autocalibrating partially parallel acquisitions (GRAPPA). Magn Reson Med 2002;47:1202–1210.